Revista Brasileira de Geofísica
RBGf
Brazilian Journal of Geophysics

Revista Brasileira de Geofísica (2011) 29(4): 811-829

ISSN 0102-261X
www.scielo.br/rbg

SPATIAL VARIATION OF ANGLE-DEPENDENT IMPEDANCE THROUGH A THIN-LAYERED OIL RESERVOIR

José Sampaio de Oliveira and Jorge Leonardo Martins

Recebido em 16 setembro, 2010 / Aceito em 24 outubro, 2011
Received on September 16, 2010 / Accepted on October 24, 2011

ABSTRACT. The P-wave elastic impedance (EI) concept is currently used as a complementary petrophysical parameter for the characterization of oil and gas reservoirs. In this paper, we construct maps representing the spatial variation of isotropic and anisotropic EI at a specific depth through a turbiditic oil-producing reservoir. EI is thus used here not for calibration and inversion of seismic data at farther offsets as firstly introduced, but as an original application of a novel petrophysical concept. As long as bulk density, seismic velocities and incidence angle are common variables in the isotropic and anisotropic EI formulas, we used geophysical measurements at the surroundings of 39 wells drilled through the reservoir formation in order to generate isotropic and anisotropic EI maps. The reservoir inner structure consists of fine layering, allowing us to approximate the formation to a transverse isotropic medium with vertical axis of symmetry (VTI medium) for anisotropic EI map construction. We then applied the Backus-averaging technique for estimating VTI elastic stiffness logs from the well log measurements through the reservoir formation. For the construction of the maps, we implemented an interpolation process incorporating a robust inverse-distance square-weighted interpolator into a search radius scheme. In this scheme, only control points inside a distance specified *a priori* are considered in the interpolation process. The resulting EI maps for incidence angles of 0°, 20° and 40°, at 3080 m depth, reveal zones of fine layering around certain wells. We observed that seismic anisotropy induced by fine layering is pronounced in these zones, coinciding with low oil-producing intervals. At the same selected depth of the reservoir formation, the remaining parts of the maps show a weak strength of VTI anisotropy.

Keywords: geophysical well logs, elastic impedance, seismic anisotropy, Backus-averaging, spatial data interpolation, Namorado reservoir.

RESUMO. O conceito de impedância elástica (EI) da onda compressional é atualmente usado como um parâmetro petrofísico complementar para a caracterização de reservatórios de petróleo e gás. Neste artigo, construímos mapas que representam a variação espacial da EI isotrópica e anisotrópica a uma profundidade específica através de um reservatório turbidítico produtor de petróleo e gás. EI é então usada aqui não para calibração e inversão de dados sísmicos de grandes afastamentos como proposto originalmente, mas como uma aplicação original de um conceito petrofísico novo. Uma vez que densidade efetiva, velocidades sísmicas e ângulo de incidência são variáveis comuns nas fórmulas isotrópica e anisotrópica da EI, usamos registros geofísicos nas vizinhanças de 39 poços perfurados através da formação que contém o reservatório a fim de gerar mapas isotrópicos e anisotrópicos de EI. A estrutura interna do reservatório consiste de camadas delgadas, o que nos permitiu aproximar a formação a um meio transversalmente isotrópico com eixo de simetria vertical (meio TIV) para construção dos mapas de EI anisotrópica. Dessa forma, aplicamos a técnica da média de Backus para estimativa dos perfis de rigidezas elásticas TIV a partir de registros de perfis de poços através da formação do reservatório. Para a construção dos mapas, implementamos um processo de interpolação incorporando um robusto interpolador de distância inversa com pesos quadráticos em um esquema de "raio de procura". Nesse esquema, somente pontos de controle dentro de uma distância especificada *a priori* são considerados no processo de interpolação. Os mapas resultantes da EI para ângulos de incidência de 0°, 20° e 40°, numa profundidade de 3080 m, revelam zonas de camadas delgadas ao redor de certos poços. Observamos que a anisotropia sísmica induzida por camadas delgadas é marcante nessas zonas, coincidindo com intervalos de baixa produção de óleo. Na mesma profundidade selecionada para a formação que contém o reservatório, as demais partes dos mapas mostram uma intensidade fraca de anisotropia TIV.

Palavras-chave: perfis geofísicos de poços, impedância elástica, anisotropia sísmica, média de Backus, interpolação espacial de dados, reservatório Namorado.

Coordenação da Área de Geofísica, Observatório Nacional, Ministério da Ciência e Tecnologia, Rua Gal. José Cristino, 77, São Cristóvão, 20921-400 Rio de Janeiro, RJ, Brazil. Phone: +55(21) 3504-9233; Fax: +55(21) 2580-7081 – E-mails: sampaio@on.br; jlmartins@on.br

INTRODUCTION

The characterization of reservoir formations benefits mainly from continuous measurements of physical properties at well locations by using geophysical logging tools (Ellis & Singer, 2007). However, although the measurements captured by fundamental logging tools are essential for reservoir interpretation, well logs can provide several additional physical properties to interpreters (Dewan, 1983). For example, interpretation of lithology logs discriminates porous and non-porous intervals. In addition, shaliness depth variation can be estimated from these lithology logs by using a suitable empirical formula (Larionov, 1969). Further integrated interpretation of porosity logs, namely, bulk density, neutron porosity and sonic logs, can minimize uncertainty in porosity estimation (Ellis & Singer, 2007), while identification of fluids in porous intervals is preferentially performed through electrical resistivity logs. In this instance, application of electrical resistivity empirical models for clay-free and/or shaly formations leads to the estimation of fluid saturation (Worthington, 1985). Nevertheless, the local information on physical properties gathered by well logs is applicable only to lithologies in the vicinity of the borehole. If only well logs are used in the correlation, the lack of information between wells yields a poor interpretation on possible discontinuities of lithologies. As there is a strong need for interpreting lithotypes continuity through the reservoir formation, the most suitable procedure is to generate maps representing the horizontal spatial variation of physical properties between wells.

Any well-logged or log-derived physical property can be input in the interpolation process for map generation. For example, using geophysical measurements around 39 vertical wells drilled in the Namorado oil field, Campos basin, Brazil, Adriano (2007) implemented a methodology for constructing depth maps showing the spatial variation of total porosity and shaliness. By applying basic interpretation formulas, bulk density and gamma-ray logs allowed estimating total porosity and shaliness logs, respectively, in the vicinity of all 39 wells. Application of the inverse-distance interpolation formula studied in Weber & Englund (1992; 1994) produced total porosity and shaliness depth maps through the Namorado reservoir formation. Comparison of both maps guided interpretation of the continuity of main lithologies forming the reservoir, suggesting possible locations for drilling additional production wells. The work of Augusto (2009) represents a further example of depth map generation from log-derived rock properties. In this instance, the well log data set of the Namorado reservoir allowed for constructing maps of P-wave acoustic impedance, normal-incidence reflection coefficients and synthetic seismic amplitudes. In comparison to the maps in Adriano (2007), the higher degree of confidence achieved in Augusto (2009) maps is due to the incorporation of a search radius scheme into the interpolation process.

In this paper, we implemented a methodology for constructing horizontal spatial variations of isotropic and anisotropic elastic impedance (EI) in the Namorado reservoir formation. The concept of isotropic P-wave EI was originally introduced by Connolly (1998) as a tool for investigating amplitude-*versus*-offset (AVO) seismic anomalies at farther incidences. Besides being applied in the calibration and inversion of seismic data, EI is also presented as a petrophysical parameter similar to acoustic impedance (AI). This property is also shared by the anisotropic P-wave EI formula derived in Martins (2006), which incorporated seismic anisotropy effects of arbitrary symmetry into Connolly (1999) isotropic approach. EI thus represents an additional rock physical property of importance in reservoir characterization, because it allows investigating seismic anisotropy effects. Bulk density, seismic velocities and angle of incidence are common parameters of the EI formulas. However, the elastic stiffnesses and an azimuthal direction are needed in Martins (2006) anisotropic EI approach. Before generating the EI maps, we prepared the Namorado reservoir well log data set by selecting the bulk density and P-wave sonic log measurements used in Augusto (2009). The absence of full-wave sonic logs in the data set led us to apply the method described in Lee (2006) for estimating S-wave velocities in the Namorado reservoir formation. Because of the fine-layering character of the formation containing the reservoir, we approximated the sedimentary column to a transverse isotropic medium with vertical axis of symmetry (i.e., a VTI medium). As the layer induced VTI anisotropy is the result of Backus-averaging effective medium theory (Backus, 1962; Stovas et al., 2006; Bayuk et al., 2008), we used this averaging technique to construct VTI stiffness logs from the Namorado reservoir well log data set. We then generated isotropic and VTI EI maps at a specific depth through the Namorado reservoir using the same interpolator and search radius scheme adopted in Augusto (2009). In the following, we present a summary of the methodology as well as the resulting horizontal spatial variation of EI through the Namorado reservoir. Because the anisotropic EI formula was firstly introduced by Martins (2006) with no actual data example, the results in the next sections are therefore a novel application of a new petrophysical concept.

METHODOLOGY

In this section we present the steps for constructing isotropic and anisotropic P-wave EI maps from geophysical well logs through

a turbiditic oil-bearing reservoir in Campos basin, Brazil. The original isotropic P-wave EI equation was presented by Connolly (1999) and refined by Whitcombe (2002) and Martins (2003). Incorporation of arbitrary-symmetry anisotropy into the P-wave EI formula is described in Martins (2006). This paper deals only with VTI symmetry, that is, we assume the formation in which the reservoir is inserted as a transversely isotropic (TI) medium having axis of symmetry oriented along x_3 direction. To estimate the effective VTI stiffnesses, we applied the effective medium theory proposed in Backus (1962). The interpolator for constructing the EI maps are described at the end of the section. Our methodology consists of: (1) preparation of bulk density and sonic logs, (2) estimation of VTI stiffnesses from well logs, and (3) generation of isotropic and anisotropic EI maps from interpolation. In the following, we present a summarized description of the well logs, the equations for EI calculation, the formulas for effective VTI stiffnesses estimation and the interpolator for construction of the EI maps.

Well log data set preparation

We generated isotropic and anisotropic EI maps using bulk density and sonic log measurements from vertical wells through the Namorado oil field, offshore Campos basin, Brazil. This oil field is located 80 km offshore the Brazilian coast, extending over an area of nearly 24 km^2. The thickness of the water layer in the region varies from 140 to 250 m. The facies of this turbiditic reservoir correspond to poorly consolidated sandstones in the sedimentary interval from 2940 to 3300 m depth of the upper Macaé formation. The sandstone reservoirs alternate with thin layers of organic and radioactive shales, siltstones and calcilutites (Tigre & Lucchesi, 1986).

In Figure 1, the structural map of the Namorado oil field shows the main production and development wells drilled in the area. The spatial geometry of the reservoir resembles a mini-horst in which most wells were drilled in the main block. We selected the geophysical logs from 39 wells located in this main portion of the reservoir. The logs of interest are the bulk density and the velocity logs, the latter extracted from sonic logs. With these measurements, we constructed logs of effective VTI stiffnesses (see subsection on effective VTI stiffnesses estimation in the following) for subsequent calculation of anisotropic EI logs.

The whole set of selected wells holds measurements of physical properties (i.e., bulk density and P-wave sonic velocity) at each 0.15 m depth through the formation containing the Namorado reservoir. However, measurements of P-wave sonic velocities are available only at five wells of our data set, that is, wells NA 1A, NA 2, NA 4, RJS 19 and RJS 42. In addition, this old exploration area has no information on measurements of S-wave velocities. In order to estimate P-wave velocities in the additional 34 wells, we used the empirical formulas proposed in Augusto et al. (2007), Augusto & Martins (2008, 2009). These authors implemented a regression analysis methodology based on the concept of areas of influence. An empirical formula was attributed to a predefined area of influence, to which an individual well containing P-wave velocity measurements was linked. In wells within the area of influence with no velocity information, estimation of P-wave velocities was performed by using the corresponding empirical relation. To complete the well log data set, we used the methodology proposed in Lee (2006) for estimating S-wave velocity logs from the empirically-estimated P-wave velocity logs in Augusto (2009) and Augusto & Martins (2009). The basic relations for estimating S-wave velocities can be found in the first part of the Appendix.

Construction of isotropic EI logs followed the preparation the Namorado reservoir well log data set described above. The formulas for calculation of isotropic and anisotropic EI logs are presented in the next section.

Isotropic and anisotropic EI formulas

Acoustic impedance (AI) is defined as the product of bulk density ρ multiplied by phase velocity α, that is,

$$\mathrm{AI} = \rho\,\alpha, \tag{1}$$

where α denotes P-wave velocity. So, from now on, AI is referred to as P-wave acoustic impedance.

AI represents a rock attribute used as diagnostic property in petrophysical analysis from well logs (Dewan, 1983; Ellis & Singer, 2007) and in seismic interpretation (Mitchum et al., 1977; Yilmaz, 2001). Moreover, AI is the link between calibration and inversion of seismic data in well log based amplitude-*versus*-offset (AVO) investigations (Castagna et al., 1993; Castagna et al., 1998). An AI log is used in the calibration process for generating a corresponding normal-incidence synthetic seismogram. The same AI log is used for constraining inversion of post-stack seismic data. Nevertheless, calibration and inversion of seismic data using AI logs are limited to near-offset seismic data, preventing investigation of typical classes of AVO anomalies (Rutherford & Williams, 1989) at farther incidences.

The study of AVO anomalies can be performed using the concept of elastic impedance (EI). Connolly (1998) introduced the isotropic P-wave EI equation in order to make possible calibration and inversion of pre-stack seismic data. Below, the original

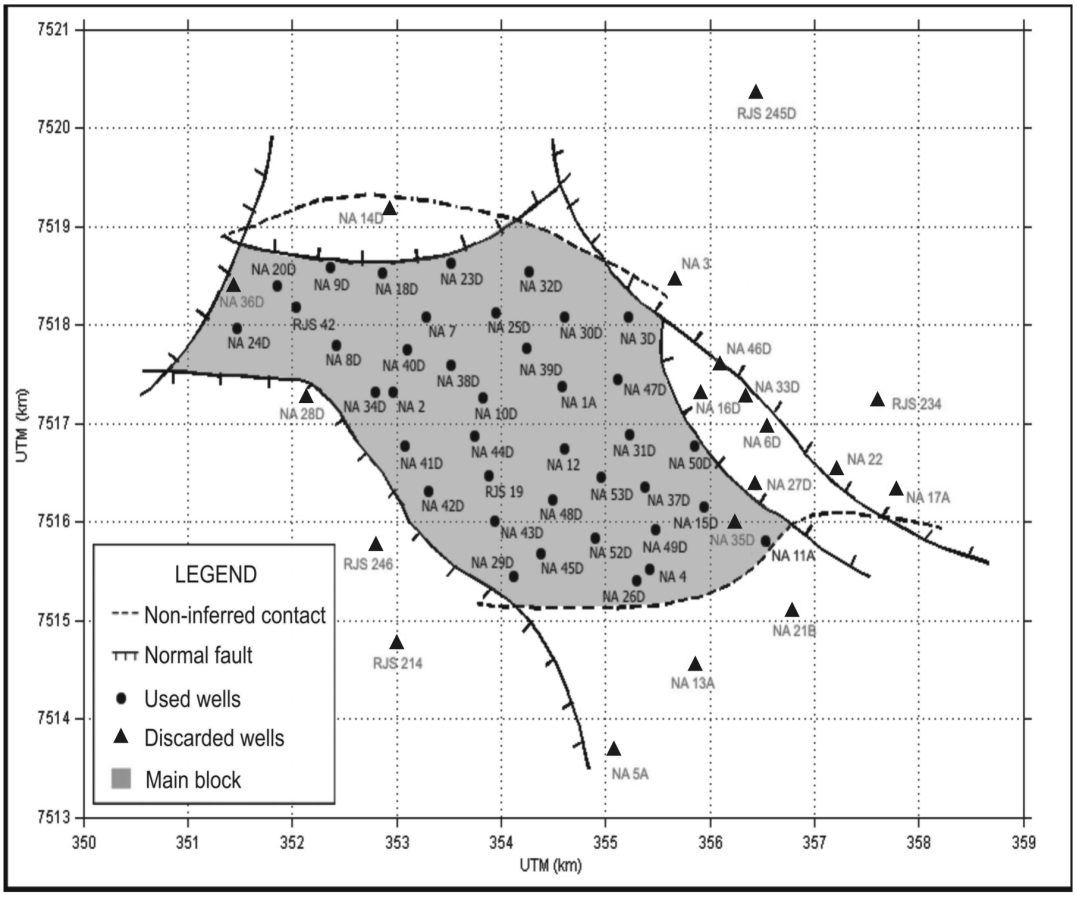

Figure 1 – Structural map of Namorado oil field, offshore Campos basin, Brazil. This figure shows the main production and development vertical wells drilled in the area. Black dots assign wells containing the geophysical logs used in this work. The top of the reservoir coincides nearly with the onset of the Macaé formation in Campos basin. The main block is the area of interest for generation of EI maps. Modified from Augusto (2009).

EI equation derived in Connolly (1999) is written slightly modified

$$\mathrm{EI}(\theta) = \rho\alpha \left(\alpha^{\tan^2\theta}\, \mathrm{G}^{-\xi}\right). \qquad (2)$$

In Eq. (2) the term G denotes shear-wave (S-wave) modulus, $\mathrm{G} = \rho\beta^2$, with β representing S-wave velocity. The parameter ξ is also function of incidence phase angle θ, $\xi \equiv \xi(\theta) = 4\mathrm{k}_1 \sin^2\theta$, where constant k_1 is defined using average values of P- and S-wave velocities, $\mathrm{k}_1 = (\bar{\beta}/\bar{\alpha})^2$. Therefore, analysis of the isotropic EI formula yields two conclusions. First, inserting $\theta = 0°$ into Eq. (2), it follows that $\mathrm{EI}(0°) = \mathrm{AI}$. Thus, EI can be considered as a rock property analogous to AI, but for varying incidences. Taking into account calibration and inversion processes using fundamental well logs, EI replaces AI. That is: an EI log allows calibrating seismic data at farther incidences, while the same EI log can be used for constraining the inversion of pre-stack seismic data (Connolly, 1999). The second conclusion from Eq. (2) refers to its dimensionality dependence on the incidence phase angle θ. VerWest et al. (2000) and VerWest (2004) inserted a different approximation for the PP-wave reflection ($\mathrm{R_{PP}}$) coefficients into Connolly's (1999) mathematical formalism, obtaining a normalized version of the EI formula which requires a reference density. Whitcombe (2002) and Martins (2003) decided for an approach which incorporates normalizing constants into Connolly's (1999) mathematical formalism, resulting in the following normalized version of the EI equation:

$$\mathrm{EI}(\theta) = \mathrm{EI}_0 \left(\frac{\rho\alpha}{\rho_0\alpha_0}\right)\left(\frac{\alpha}{\alpha_0}\right)^{\tan^2\theta}\left(\frac{\mathrm{G}}{\mathrm{G}_0}\right)^{-\xi}. \qquad (3)$$

Selection of normalizing constants ρ_0, α_0, β_0, $\mathrm{G}_0 = \rho_0\beta_0^2$ and $\mathrm{EI}_0 = \rho_0\alpha_0$ at a specific depth facilitates correlation of AI and EI in the same units (Whitcombe, 2002). However, although Eq. (3) is no longer unity dependent, its use is still limited to isotropic media. In oil and gas exploration, there is a demonstrated need for including anisotropic effects into the methodologies (Helbig, 1994).

In order to incorporate effects of anisotropy into the EI formula, Martins (2006) used the first-order approximation for R_{PP} coefficients derived in Vavryčuk & Pšenčík (1998). This anisotropic approximation for the coefficients is formed by the sum of the linear isotropic R_{PP} approximation in Aki & Richards (1980) and a term representing the first-order perturbation to anisotropy. Thus, Vavryčuk & Pšenčík's (1998) coefficient formula applies for weak-contrast interfaces separating weakly anisotropic media with arbitrary symmetry. Use of this R_{PP} approximation into a slightly modified version of Connolly's (1999) formalism yields an anisotropic EI equation which has the same properties of Vavryčuk & Pšenčík's (1998) R_{PP} coefficient. The anisotropic EI equation is presented in Martins (2006) as a product of two terms:

$$\mathrm{EI}(\varphi,\theta) = \mathrm{EI}(\theta)\ \Delta\mathrm{EI}(\varphi,\theta). \tag{4}$$

The first term $\mathrm{EI}(\theta)$ corresponds to the isotropic EI formula in Eq. (3), while the second term $\Delta\mathrm{EI}(\varphi,\theta)$ represents an exponential correction attributable to weak anisotropy,

$$\Delta\mathrm{EI}(\varphi,\theta) = \exp\left[\, 2\int d\,\mathrm{R_{PP}}(\varphi,\theta)\,\right]. \tag{5}$$

After integrating and conveniently setting the integration constant to zero, Martins (2006) demonstrates that the argument of this exponential correction term contains the whole anisotropy information (i.e., the elastic stiffnesses and the azimuthal direction φ), namely

$$\begin{aligned} &2\int d\,\mathrm{R_{PP}}(\varphi,\theta) \\ &\equiv \alpha^2\,\mathrm{k_2}\,\big\{\,\epsilon_z\cos^2\theta + [\,(\delta_x - 8(\beta/\alpha)^2\,\gamma_x)\cos^2\varphi \\ &\quad + (\delta_y - 8(\beta/\alpha)^2\,\gamma_y)\sin^2\varphi \\ &\quad + (\chi_z - 4(\beta/\alpha)^2\,\epsilon_{45})\sin 2\varphi\,]\ \sin^2\theta \\ &\quad + [\,\epsilon_x\cos^4\varphi + \epsilon_y\sin^4\varphi + \frac{1}{4}\,\delta_z\ \sin^2 2\varphi \\ &\quad + (\epsilon_{16}\cos^2\varphi + \epsilon_{26}\sin^2\varphi)\sin 2\varphi\,]\ \sin^2\theta\ \tan^2\theta\,\big\}, \end{aligned} \tag{6}$$

where $\mathrm{k_2} = 1/\bar{\alpha}^2$. See in the second part of the Appendix the main steps to derive Eq. (6). The weak anisotropy (WA) parameters (i.e., ϵ_x, ϵ_y, ϵ_z, ϵ_{16}, ϵ_{26}, ϵ_{45}, γ_x, γ_y, δ_x, δ_y, δ_z and χ_z) introduced in Mensch & Rasolofosaon (1997) and Pšenčík & Gajewski (1998), contain information on the elements of the corresponding density-normalized elastic matrix, $\mathbf{A}_{ij} = \mathbf{c}_{ij}/\rho$ (condensed notation applied). Further, α and β become parameters which can be selected in such a way that some WA parameters are zeroed. As a result, Pšenčík & Gajewski (1998) redefine α and β as the P- and S-wave reference velocities, respectively. Note that Martins (2008) refers to EI as the angle-dependent impedance of an anisotropic rock, due to the presence of the incidence phase angle θ and the azimuthal direction φ in the argument of Eq. (6).

Specifying Eq. (6) for VTI symmetry, $A_{11} = A_{22}$, $A_{13} = A_{23}$, A_{33}, $A_{44} = A_{55}$, A_{66} and $A_{12} = A_{11} - 2\,A_{66}$. The WA parameters then reduce to $\chi_z = \epsilon_{16} = \epsilon_{26} = \epsilon_{45} = 0$, $\epsilon_y = \epsilon_x$, $\delta_y = \delta_x$, $\delta_z = 2\,\epsilon_x$ and $\gamma_y = \gamma_x$, yielding (Martins, 2006)

$$\begin{aligned} &2\int d\,\mathrm{R_{PP}}(\theta) \ \equiv\ \alpha^2\,\mathrm{k_2}\,\big[\,\epsilon_z\ \cos^2\theta \\ &+ (\delta_x - 8(\beta/\alpha)^2\,\gamma_x)\ \sin^2\theta + \epsilon_x\ \sin^2\theta\ \tan^2\theta\,\big]. \end{aligned} \tag{7}$$

As observed, the argument of the correction attributable to weak anisotropy for VTI symmetry consistently exhibits no dependence on azimuths φ, i.e., $\Delta\mathrm{EI}(\varphi,\theta) \equiv \Delta\mathrm{EI}^{\mathrm{vti}}(\theta)$. In addition, the WA parameters ϵ_z, ϵ_x, δ_x and γ_x (Pšenčík & Gajewski, 1998),

$$\epsilon_z = \frac{A_{33} - \alpha^2}{2\alpha^2}, \quad \epsilon_x = \frac{A_{11} - \alpha^2}{2\alpha^2}, \tag{8}$$

$$\delta_x = \frac{A_{13} + 2A_{55} - \alpha^2}{\alpha^2}, \quad \gamma_x = \frac{A_{55} - \beta^2}{2\beta^2}, \tag{9}$$

control the specification of the EI equation in VTI media. As mentioned above, selection of reference P- and S-wave velocities α and β are critical for calculating the WA parameters. For instance, assuming in Eqs. (8) and (9) $\alpha^2 = A_{33}$ and $\beta^2 = A_{55}$, only ϵ_x and δ_x will control the correction of the EI equation for VTI symmetry.

From now on, the isotropic EI formula in Eq. (3) will be referred to as $\mathrm{EI}(\theta) \equiv \mathrm{EI}^{\mathrm{iso}}(\theta)$. In turn, because we consider rocks with VTI symmetry, the azimuthal direction φ is dropped from the anisotropic EI formula and Eq. (4) will be referred to as $\mathrm{EI}(\varphi,\theta) \equiv \mathrm{EI}^{\mathrm{vti}}(\theta)$. As observed in Eq. (7), estimation of effective VTI stiffnesses is required for computing the argument of the correspondent correction term $\Delta\mathrm{EI}^{\mathrm{vti}}(\theta)$.

Effective VTI stiffnesses

Under assumption that the dominant wavelength obtained in conventional seismics is large compared to the layer thicknesses, a stack of alternating sequence of small-thickness homogeneous elastic isotropic and/or anisotropic layers exhibits VTI anisotropy behavior (Postma, 1955; Backus, 1962). Applying an upscaling process, the effective VTI stiffnesses of such layered structure can be estimated from bulk density and full-wave sonic logs. In this way, weighted arithmetic average formulas allows the calculation

of the five effective VTI stiffnesses within a specified frequency-dependent window length (Liner & Fei, 2006; Stovas et al., 2006; Bayuk et al., 2008; Tiwary et al., 2009).

Representing $\mathrm{h_i}$ and $\mathrm{x_i}$ as the thickness and the elastic stiffness, respectively, of the i-th layer, the weighted arithmetic averages $\langle\, x^{(\mathrm{i})} \,\rangle$ and $\langle\, 1/x^{(\mathrm{i})} \,\rangle$ are defined as

$$\langle\, x^{(\mathrm{i})} \,\rangle = \frac{\sum_{\mathrm{i}=1}^{\mathbf{n}} (\mathrm{h_i}\, \mathrm{x_i})}{\sum_{\mathrm{i}=1}^{\mathbf{n}} \mathrm{h_i}}, \quad \text{and}$$
$$\left\langle \frac{1}{x^{(\mathrm{i})}} \right\rangle = \frac{\sum_{\mathrm{i}=1}^{\mathbf{n}} (\mathrm{h_i}/\mathrm{x_i})}{\sum_{\mathrm{i}=1}^{\mathbf{n}} \mathrm{h_i}}, \tag{10}$$

in which the number of layers in the stack is denoted by $\mathbf{n}$. The stiffnesses of the effective VTI medium c_{11}^{vti}, c_{13}^{vti}, c_{33}^{vti}, c_{55}^{vti} and c_{66}^{vti} can be estimated using the so-called Backus-averaging formulas (Backus, 1962)

$$\frac{1}{c_{33}^{\mathrm{vti}}} = \left\langle \frac{1}{c_{33}^{(\mathrm{i})}} \right\rangle, \quad \frac{1}{c_{55}^{\mathrm{vti}}} = \left\langle \frac{1}{c_{55}^{(\mathrm{i})}} \right\rangle,$$
$$c_{66}^{\mathrm{vti}} = \left\langle c_{66}^{(\mathrm{i})} \right\rangle, \frac{c_{13}^{\mathrm{vti}}}{c_{33}^{\mathrm{vti}}} = \left\langle \frac{c_{13}^{(\mathrm{i})}}{c_{33}^{(\mathrm{i})}} \right\rangle, \tag{11}$$
$$c_{11}^{\mathrm{vti}} - \frac{[\, c_{13}^{\mathrm{vti}} \,]^2}{c_{33}^{\mathrm{vti}}} = \left\langle c_{11}^{(\mathrm{i})} - \frac{[\, c_{13}^{(\mathrm{i})} \,]^2}{c_{33}^{(\mathrm{i})}} \right\rangle.$$

In order to complete the VTI elastic matrix, the stiffness c_{12}^{vti} can then be calculated as $c_{12}^{\mathrm{vti}} = c_{11}^{\mathrm{vti}} - 2\, c_{66}^{\mathrm{vti}}$. For isotropic layers, the following stiffnesses must be substituted in Eqs. (11): $c_{12}^{(\mathrm{i})} = c_{13}^{(\mathrm{i})} = c_{23}^{(\mathrm{i})} = \lambda^{(\mathrm{i})}$, $c_{11}^{(\mathrm{i})} = c_{22}^{(\mathrm{i})} = c_{33}^{(\mathrm{i})} = \lambda^{(\mathrm{i})} + 2\,\mu^{(\mathrm{i})}$ and $c_{44}^{(\mathrm{i})} = c_{55}^{(\mathrm{i})} = c_{66}^{(\mathrm{i})} = \mu^{(\mathrm{i})}$. Using the i-th log measurement of bulk density ρ_{i}, P-wave sonic velocity α_{i} and S-wave sonic velocity β_{i}, corresponding calculation of Lamé parameters are performed with $\lambda_{\mathrm{i}} = \rho_{\mathrm{i}}(\alpha_{\mathrm{i}}^2 - 2\beta_{\mathrm{i}}^2)$ and $\mu_{\mathrm{i}} = \rho_{\mathrm{i}}\beta_{\mathrm{i}}^2$. The first of the equations in (10) then allows estimating $\langle\, \lambda^{(\mathrm{i})} \,\rangle$ and $\langle\, \mu^{(\mathrm{i})} \,\rangle$.

Although the formulas above are routinely applied assuming isotropic layers (Postma, 1955), anisotropic layers are also allowed (Backus, 1962). For instance, Liner & Fei (2006) proposed a methodology to incorporate anisotropic layers in the Backus-averaging process. The number of samples for the averaging window is also discussed in Liner & Fei (2006), which conclude that the window length must be less than or equal to one-third of the minimum dominant wavelength. Based on this result, the use of a 51-sample averaging window allowed us to enhance thin-layer anomalies in the effective VTI stiffness logs. Measurements of bulk density ρ_{i} provided the inputs for estimating the apparent density log $\langle\, \rho^{(\mathrm{i})} \,\rangle$ – see the first of the equations in (10), using the same length for the averaging window. Next, due to the need for density-normalized VTI stiffnesses A_{ij}^{vti} as in Eqs. (8) and (9), density-normalized VTI stiffness logs could be calculated by taking the corresponding apparent density logs. Under these assumptions, α_{i} and β_{i} above represent the i^{th} sample of a reference velocity log computed from a correspondent density-normalized stiffness log. Considering the example that follows Eqs. (8) and (9), $\alpha_{\mathrm{i}}^2 = A_{33,\mathrm{i}}^{\mathrm{vti}}$ and $\beta_{\mathrm{i}}^2 = A_{55,\mathrm{i}}^{\mathrm{vti}}$. For application of Eqs. (10) and (11), note that the log sample interval corresponds to the layer thickness $\mathrm{h_i}$. As defined in the section describing the well log data set, $\mathrm{h_i} = 0.15$ m.

Generation of EI maps

The computation of $\mathrm{EI}^{\mathrm{iso}}(\theta)$ and $\mathrm{EI}^{\mathrm{vti}}(\theta)$ logs for each well of our data set was necessary for generating EI depth maps through the Namorado reservoir. The information in these logs served as control points for the interpolation process for estimating EI in the grid cells used for discretizing the area under study.

In the gridding step, a selected region of the reservoir bounded by UTM coordinates pairs $(\mathrm{X_{min}}, \mathrm{Y_{min}})$ and $(\mathrm{X_{max}}, \mathrm{Y_{max}})$ was discretized into cells with dimensions $\mathrm{d_x}$ and $\mathrm{d_y}$. The scheme in Figure 2 depicts the result of the gridding step using squared cells. The intersection of a specified depth with the well locations formed a set of control points used for estimating EI values in the center of the discretizing cells. In Figure 2, the control points are assigned with numbers between parentheses. The center of an individual cell receives the estimative resulting from the interpolation process.

To estimate EI values in the grid cells, we developed our algorithm based on the inverse-distance estimator studied in Weber & Englund (1992; 1994). It can be shortly written as

$$\mathrm{Z_j^{r_s}} = \sum_{\mathrm{i}=1}^{\mathrm{n}} \mathrm{Z_i}\, \omega_{\mathrm{i}}^{\mathrm{r_s}}, \tag{12}$$

where $\mathrm{Z_j^{r_s}}$ denotes the estimated EI value in the j^{th} grid cell. Clearly, the estimator above depends on the search radius $\mathrm{r_s}$, which is used for selecting a set of n control points taking part in the evaluation of the weights $\omega_{\mathrm{i}}^{\mathrm{r_s}}$. Thus, $\mathrm{Z_i}$ is the EI value in the i^{th} control point inside the search radius $\mathrm{r_s}$; a corresponding $\omega_{\mathrm{i}}^{\mathrm{r_s}}$ is attributed to the i^{th} control point. The general formula for computing the weights $\omega_{\mathrm{i}}^{\mathrm{r_s}}$ has the following form

$$\omega_{\mathrm{i}}^{\mathrm{r_s}} = \frac{\left(\frac{\mathrm{r_s} - \mathrm{d_i}}{\mathrm{d_i}}\right)^{\mathrm{m}}}{\sum_{\mathrm{j}=1}^{\mathrm{n}} \left(\frac{\mathrm{r_s} - \mathrm{d_j}}{\mathrm{d_j}}\right)^{\mathrm{m}}}, \tag{13}$$

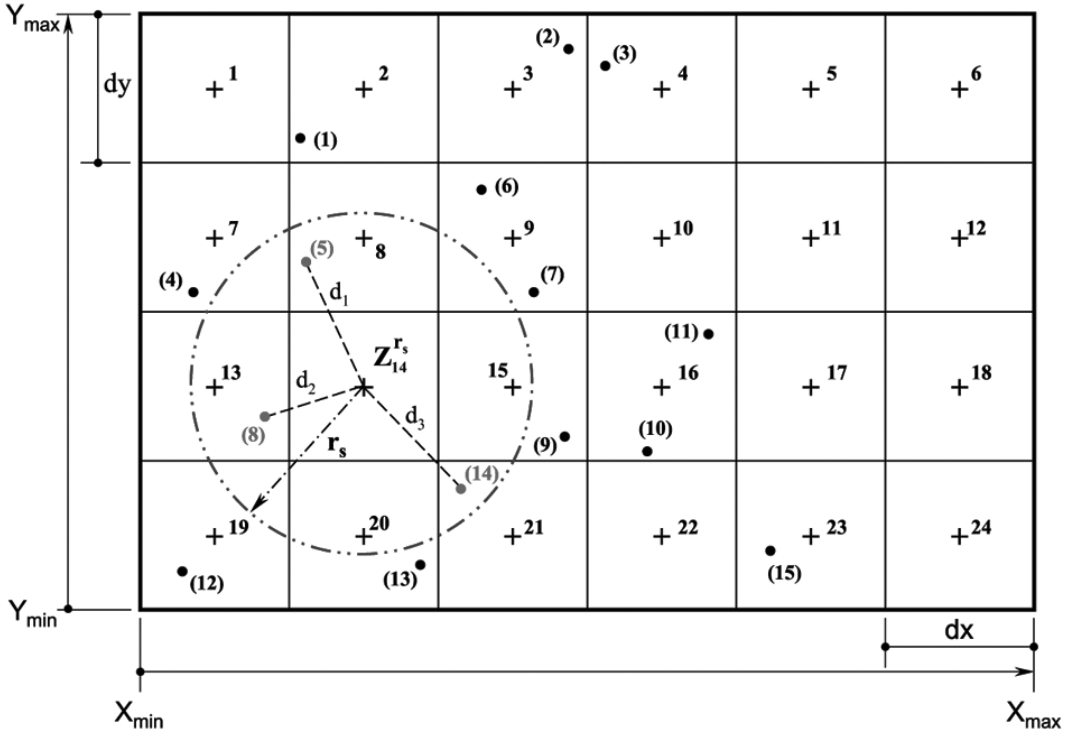

Figure 2 – Interpolation scheme for generation of EI maps. In the center of the grid cells, the symbol '+' assigns the estimated EI value. The control points are labelled with number between parentheses. The d_i's denote the distance between the center of the grid cell and the control points selected within the search radius r_s. The figure depicts a situation where three control points will take part in the interpolation process for estimating $Z_{14}^{r_s}$, which will represent the EI value interpolated in the 14^{th} grid cell.

where the distance between the center of a grid cell and i^{th} control point inside the search radius is denoted as d_i (see the gridding scheme in Fig. 2). As a result, an individual control point influences on the estimation of the EI value in the center of a grid cell through the corresponding weight $\omega_i^{r_s}$. Selecting $m = 2$, the spatial interpolator in Eq. (12) becomes an inverse-distance square-weighted interpolator (Weber & Englund, 1992; 1994).

In Eq. (13) two possible limiting situations can occur. First, a control point can be situated exactly in the circumference defined by the search radius, which gives $r_s = d_i$. The second limiting situation refers to a control point situated exactly in the center of the correspondent grid cell, i.e., $d_i = 0$. In our interpolation algorithm, we avoided the first limiting situation by considering only control points inside the circumference defined by r_s. On the other hand, to deal with the second limiting situation, we discarded control points very near the center of the grid cell having $d_i < 0.001$ m. In addition, a remarkable property of Eq. (13) is the simultaneous influence of the search radius r_s in computing the weights $\omega_i^{r_s}$ and in estimating the EI values. Because the gridded area is irregularly populated by control points, a situation may occur where the calculation of the weight is impossible, i.e., the situation when the selected search radius surrounds no control points. In order to avoid capturing no control points, we used a variable search radius during the interpolation process.

RESULTS

In order to generate maps representing the horizontal spatial variation of $EI^{iso}(\theta)$ and $EI^{vti}(\theta)$ through a specified depth of the Namorado reservoir, we selected an area from Figure 1 bounded by the UTM coordinate pairs $(X_{min} = 351, Y_{min} = 7515)$ and $(X_{max} = 357, Y_{max} = 7519)$. Thus, the EI variations in the main block of the Namorado reservoir will be inside a window with 24 km^2. In the gridding process we used square cells with dimensions $d_x = d_y = 100$ m, constraining the interpolation process to 2400 grid points. The result of the gridding process is shown in Figure 3.

As shown in Figure 1, the interpolation process for estimating EI values in the selected area relied on just 39 irregularly distributed control points. In order to deal with the resulting sparsity of control points in the discretized region, an appropriate strategy is to use the search radius varying from a maximum to a minimum value. For grid cells away from the center of the

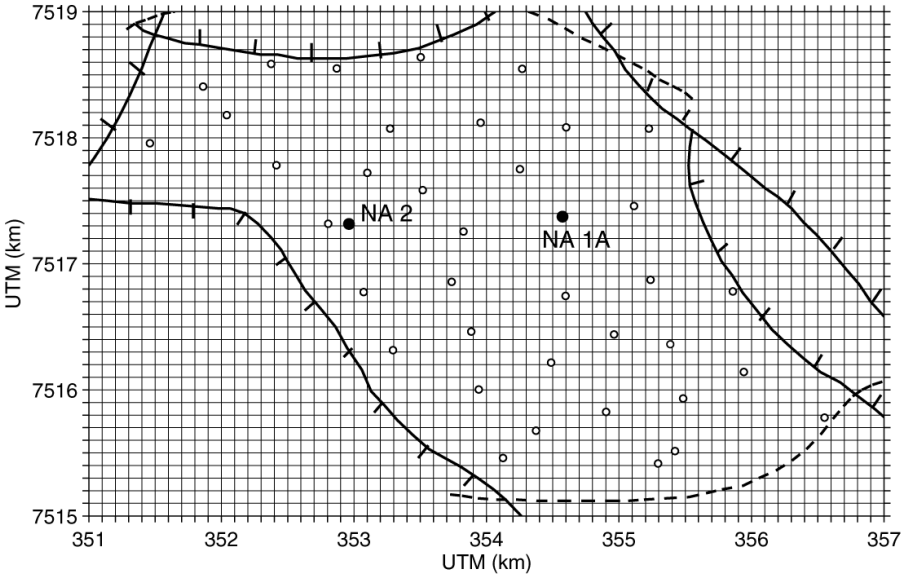

Figure 3 – Result of the gridding process over the main block of Namorado reservoir. Use of square cells with dimensions $d_x = d_y = 100$ m yielded 2400 grid points associated the centers of the grid cells. Control points taken into account in the interpolation process are marked with circles. Filled circles denote reference wells NA 1A and NA 2.

main block of the Namorado reservoir, the maximum search radius must select at least 1 control point. For grid cells near the area with greater distribution of control points, the search radius reaches the minimum. In the region bounded by the UTM coordinate pairs described above, an optimal selection for the maximum and minimum search radius are $r_s = 3.0$ km and $r_s = 1.5$ km, respectively.

Analysis of the lithology columns of two reference wells provides a criterion for selecting the depth of interest to map the spatial variation of EI through the Namorado reservoir. As shown in Figure 4, the lithology columns interpreted at wells NA 1A and NA 2 exhibit thin layers of shales and calcilutites embedded in oil-bearing sandstone intervals. The predominance of sandstones can be noticed at the vicinities of well NA 1A in Figure 4(a), while the occurrence of thin layers is more abundant at the surroundings of well NA 2 in Figure 4(b). Thus, the variation of EI around well NA 2 is expected to reflect higher VTI anisotropy effects with increasing incidence angle θ. We then decided to construct maps of the variation of $\mathrm{EI}^{\mathrm{iso}}(\theta)$ and $\mathrm{EI}^{\mathrm{vti}}(\theta)$ at the depth of 3080 m, assuming incidence angles of 0°, 20° and 40°.

For interpreting the features in the resulting EI maps, the selection of the reference velocities α and β represents an additional issue to be discussed. In Eq. (7), reference velocities are needed for computing the argument of the correction term $\Delta\mathrm{EI}^{\mathrm{vti}}(\theta)$ and subsequent calculation of $\mathrm{EI}^{\mathrm{vti}}(\theta)$. As shown in Eqs. (8) and (9), the reference velocities α and β can be selected in order to reduce some of the WA parameters ϵ_z, γ_x, ϵ_x and δ_x to zero. For instance, if vertical reference velocities $\alpha^2 = A_{33}$ and $\beta^2 = A_{44}$ are selected, then $\epsilon_z = \gamma_x = 0$ and only the WA parameters ϵ_x and δ_x will control the calculation of the correction term $\Delta\mathrm{EI}^{\mathrm{vti}}(\theta)$. However, as α and β are arbitrary parameters in the anisotropic EI equation, we used the reference velocities as $\alpha^2 = (A_{11}+A_{22}+A_{33})/3$ and $\beta^2 = (A_{44}+A_{55}+A_{66})/3$. Experiments using these reference velocities enhanced thin-layer anomalies in the final calculation of $\mathrm{EI}^{\mathrm{vti}}$ logs (see Fig. 4). As a result, nonzero WA parameters ϵ_z, γ_x, ϵ_x and δ_x controlled calculation of the correction term $\Delta\mathrm{EI}^{\mathrm{vti}}(\theta)$. Still, in order to maintain compatibility of calculations, we used α and β in the isotropic EI equation as the reference velocities for computation of the $\mathrm{EI}^{\mathrm{iso}}$ logs.

Taking into account the specified depth, angles of incidence and reference velocities as discussed above, the resulting EI maps are correspondingly displayed in Figures 5, 6 and 7. For the selected angles of incidence, the spatial distribution of heterogeneities exhibited in $\mathrm{EI}^{\mathrm{iso}}(\theta)$ and $\mathrm{EI}^{\mathrm{vti}}(\theta)$ maps shows replication of predominant features. The small differences between the $\mathrm{EI}^{\mathrm{iso}}$ and $\mathrm{EI}^{\mathrm{vti}}$ maps can be attributed to the formation weak strength of anisotropy. In other words, assuming a given incidence angle θ, the formation weak strength of seismic anisotropy yields no remarkable differences between the spatial distribution

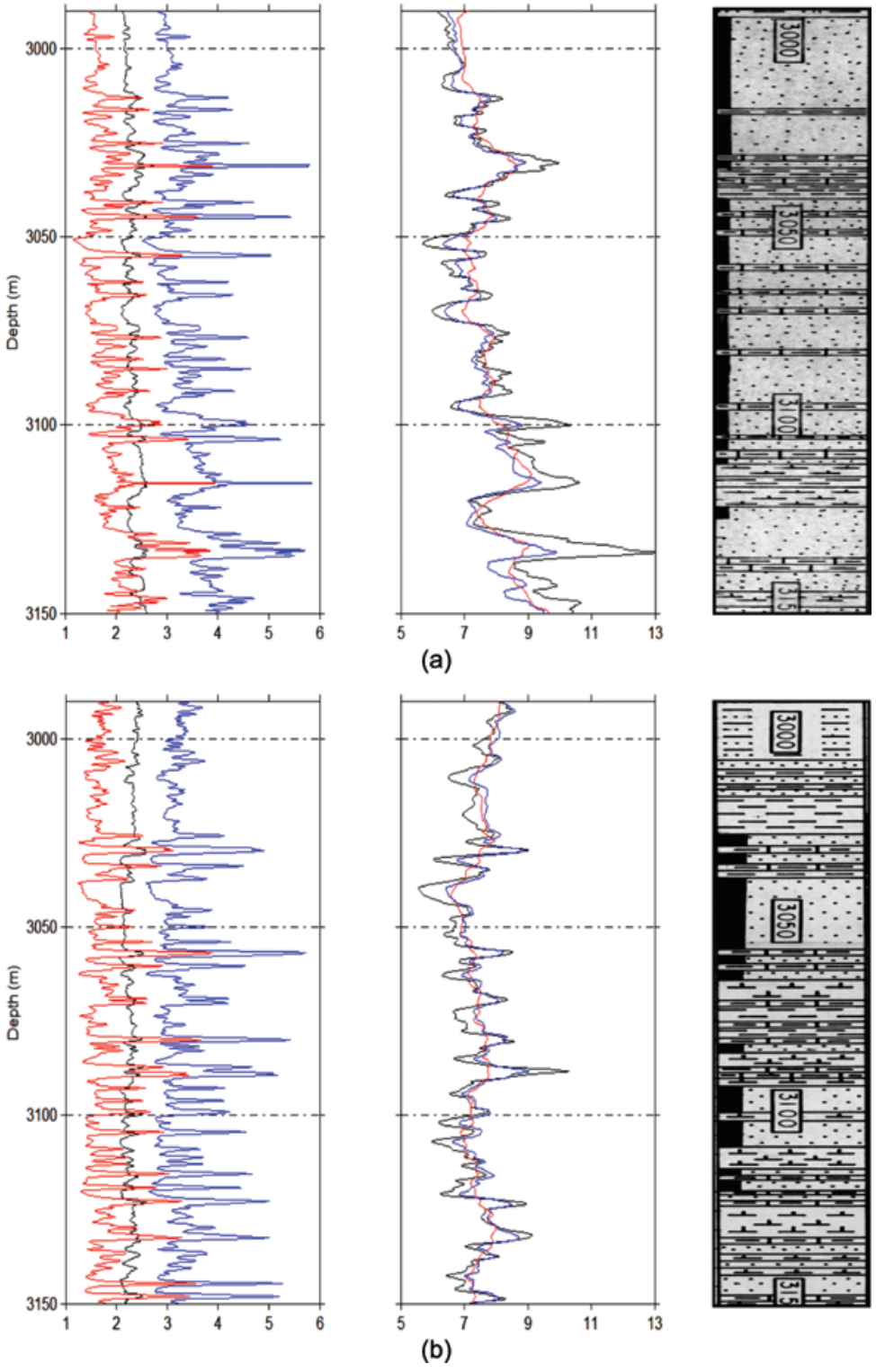

Figure 4 – Geophysical logs: (a) at well NA 1A and (b) at well NA 2 (see locations in Figs. 1 and 3). Left panel: S- and P-wave velocity (red and blue curves, respectively) in km/s, and bulk density (black curve) in g/cm^3. Central panel: impedance logs in km/s $\times$ g/cm^3: AI = $\mathrm{EI}^{\mathrm{iso}}(0°)$ (black curve), $\mathrm{EI}^{\mathrm{iso}}(30°)$ (blue curve) and $\mathrm{EI}^{\mathrm{vti}}(30°)$ (red curve). Reference velocities for computing impedance logs after application of Backus-averaging method: $\alpha^2 = (A_{11} + A_{22} + A_{33})/3$ and $\beta^2 = (A_{44} + A_{55} + A_{66})/3$. Right panel: correspondent geologic facies interpreted from cuttings and plugs. Note the good correlation between thin-layer facies and most features in the log curves.

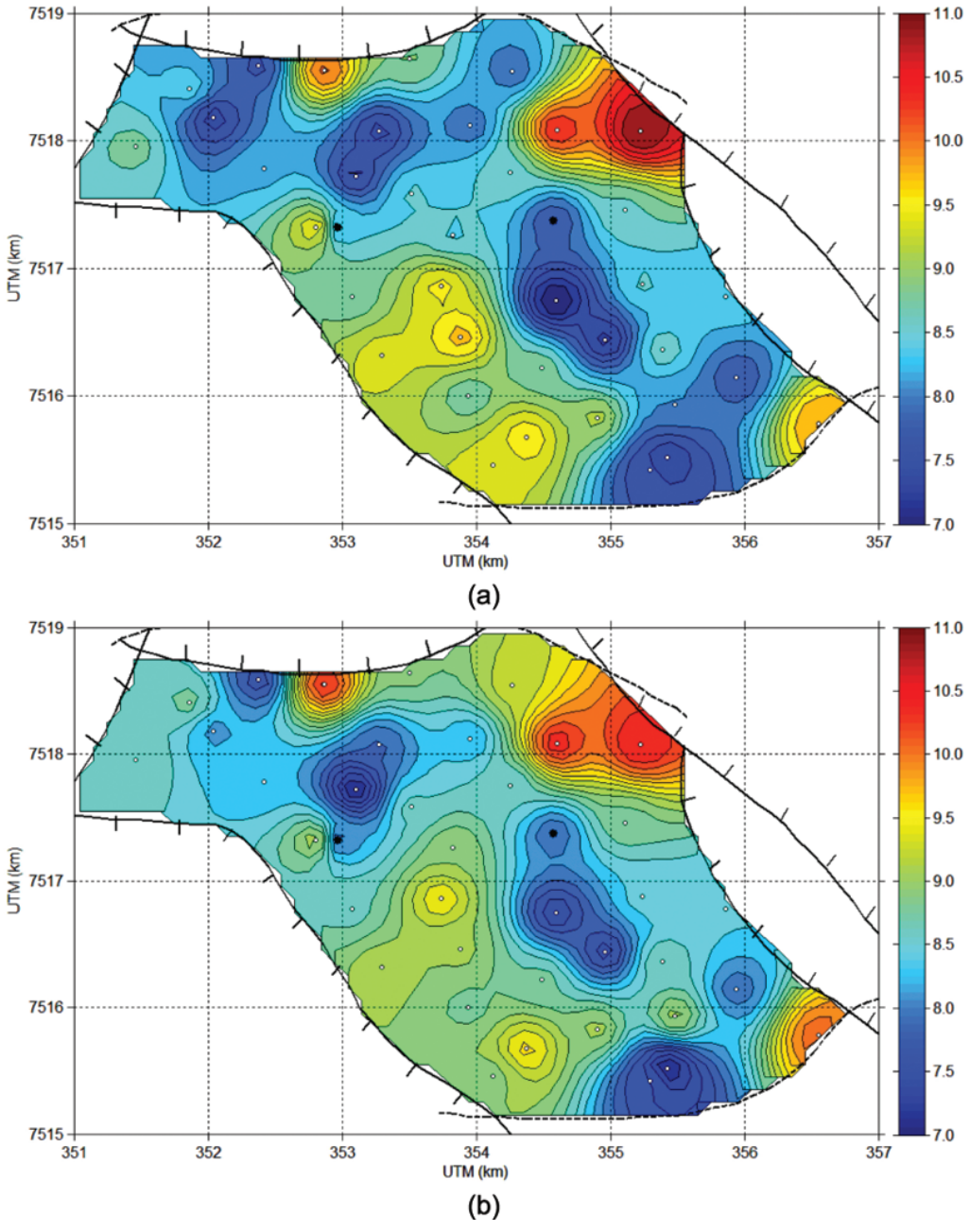

Figure 5 – Spatial variation of EI through the Namorado reservoir at 3080 m depth: (a) $\mathrm{EI}^{\mathrm{iso}}(0°)$ and (b) $\mathrm{EI}^{\mathrm{vti}}(0°)$. Filled circles denote reference wells NA 1A and NA 2 (see locations in Figs. 1 and 3). White circles are further wells drilled in the area. EI in km/s $\times$ g/cm^3.

of $\mathrm{EI}^{\mathrm{iso}}$ and $\mathrm{EI}^{\mathrm{vti}}$. Also, the selection of reference velocities contributed to the small differences in the features exhibited by the isotropic and anisotropic maps. For example, let us consider the normal-incidence maps $\mathrm{EI}^{\mathrm{iso}}(0°)$ and $\mathrm{EI}^{\mathrm{vti}}(0°)$ in Figure 5(a) and 5(b). If the reference velocities were taken as $\alpha^2 = A_{33}$ and $\beta^2 = A_{44}$, the correction term for VTI anisotropy would reduce to $\Delta\mathrm{EI}^{\mathrm{vti}}(0°) = 1$ (see details in Eqs. 5, 7, 8 and 9). Consequently, the relation $\mathrm{AI} = \mathrm{EI}^{\mathrm{iso}}(0°) = \mathrm{EI}^{\mathrm{vti}}(0°)$ would be obtained from Eqs. (3) and (4). However, as mentioned above, we assumed the reference velocities as $\alpha^2 = (A_{11}+A_{22}+A_{33})/3$ and $\beta^2 = (A_{44} + A_{55} + A_{66})/3$ for generating the normal-incidence maps $\mathrm{EI}^{\mathrm{iso}}(0°)$ and $\mathrm{EI}^{\mathrm{vti}}(0°)$. In this instance, the

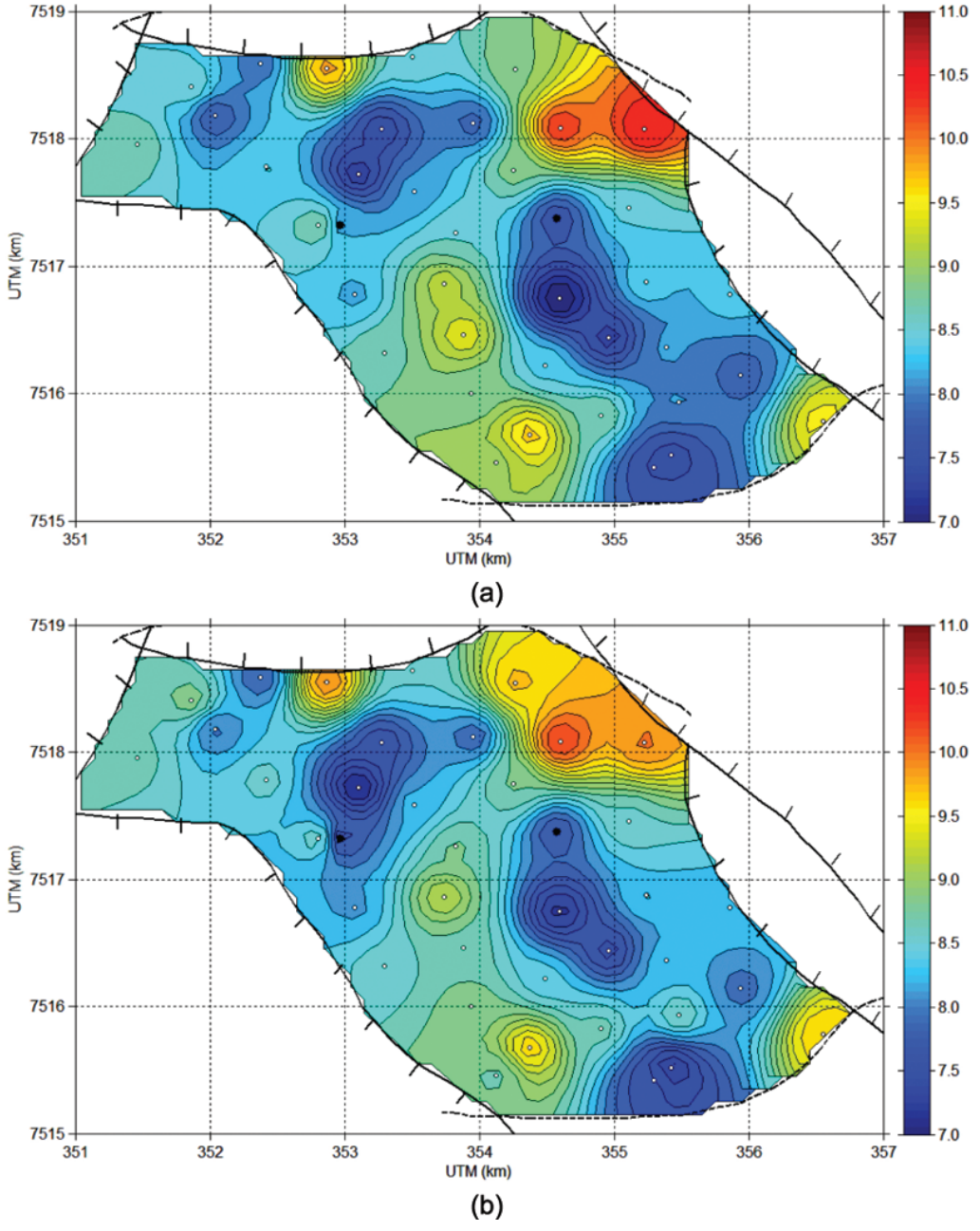

Figure 6 – Spatial variation of EI through the Namorado reservoir at 3080 m depth: (a) $\mathrm{EI}^{\mathrm{iso}}(20°)$ and (b) $\mathrm{EI}^{\mathrm{vti}}(20°)$. Filled circles denote reference wells NA 1A and NA 2 (see locations in Figs. 1 and 3). White circles are further wells drilled in the area. EI in km/s $\times$ g/cm^3.

correction term for VTI anisotropy at $\theta = 0°$ is controlled only by the WA parameter ϵ_z, i.e, $\Delta\mathrm{EI}^{\mathrm{vti}}(0°) = \exp[(\alpha^2/\bar{\alpha}^2)\,\epsilon_z]$. Hence, as long as $\mathrm{EI}^{\mathrm{iso}}(0°) \neq \mathrm{EI}^{\mathrm{vti}}(0°)$, the differences between the $\mathrm{EI}^{\mathrm{iso}}(0°)$ and $\mathrm{EI}^{\mathrm{vti}}(0°)$ maps are due to the selection of reference velocities as above.

As the incidence phase angle increases, changes of predominant features in the $\mathrm{EI}^{\mathrm{iso}}$ and $\mathrm{EI}^{\mathrm{vti}}$ maps can be clearly observed. The decrease in the magnitude of EI correlates with the observed changes in the maps. By comparing Figures 6 and 7, we note that $\mathrm{EI}^{\mathrm{vti}}$ maps experience more pronounced changes in the predominant features than the $\mathrm{EI}^{\mathrm{iso}}$ maps. As a confirmation of the formation weak strength of anisotropy, we note slight changes in the $\mathrm{EI}^{\mathrm{iso}}$ and $\mathrm{EI}^{\mathrm{vti}}$ magnitudes at the surroundings of wells NA 1A and NA 2. Surprisingly, the isotropic

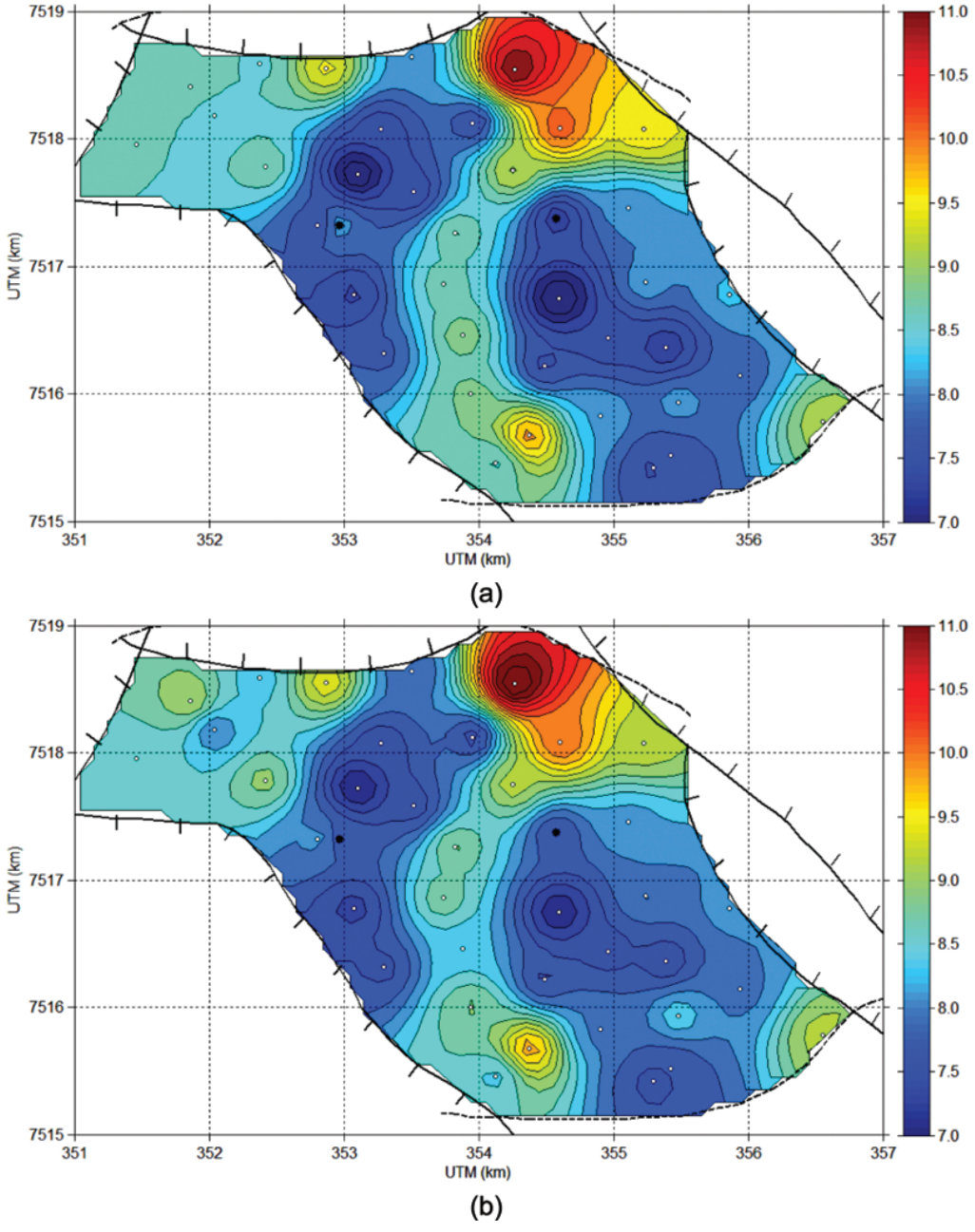

Figure 7 – Spatial variation of EI through the Namorado reservoir at 3080 m depth: (a) $\mathrm{EI}^{\mathrm{iso}}(40°)$ and (b) $\mathrm{EI}^{\mathrm{vti}}(40°)$. Filled circles denote reference wells NA 1A and NA 2 (see locations in Figs. 1 and 3). White circles are further wells drilled in the area. EI in km/s $\times$ g/cm^3.

and anisotropic maps exhibit a very distinct EI heterogeneity in the northeastern region of the Namorado reservoir at 3080 m depth. This heterogeneity continues until a very pronounced change in magnitudes at $40°$ angle of incidence. For confirmation of such abrupt changes, it would be necessary to execute well log based AVO analyses using the EI concept at far angles of incidence. Nevertheless, the maps of absolute relative residuals in EI plotted in Figure 8 help interpreting these heterogeneities as regions where VTI anisotropy effects are higher around some wells. At 3080 m depth, weak strength of VTI anisotropy applies to the remaining parts of the formation.

Table 1 contains statistical measures which help evaluating uncertainties in the generated $\mathrm{EI}^{\mathrm{iso}}$ and $\mathrm{EI}^{\mathrm{vti}}$ maps. For the computation of statistical measures, we took into account $\mathrm{EI}^{\mathrm{iso}}$ and

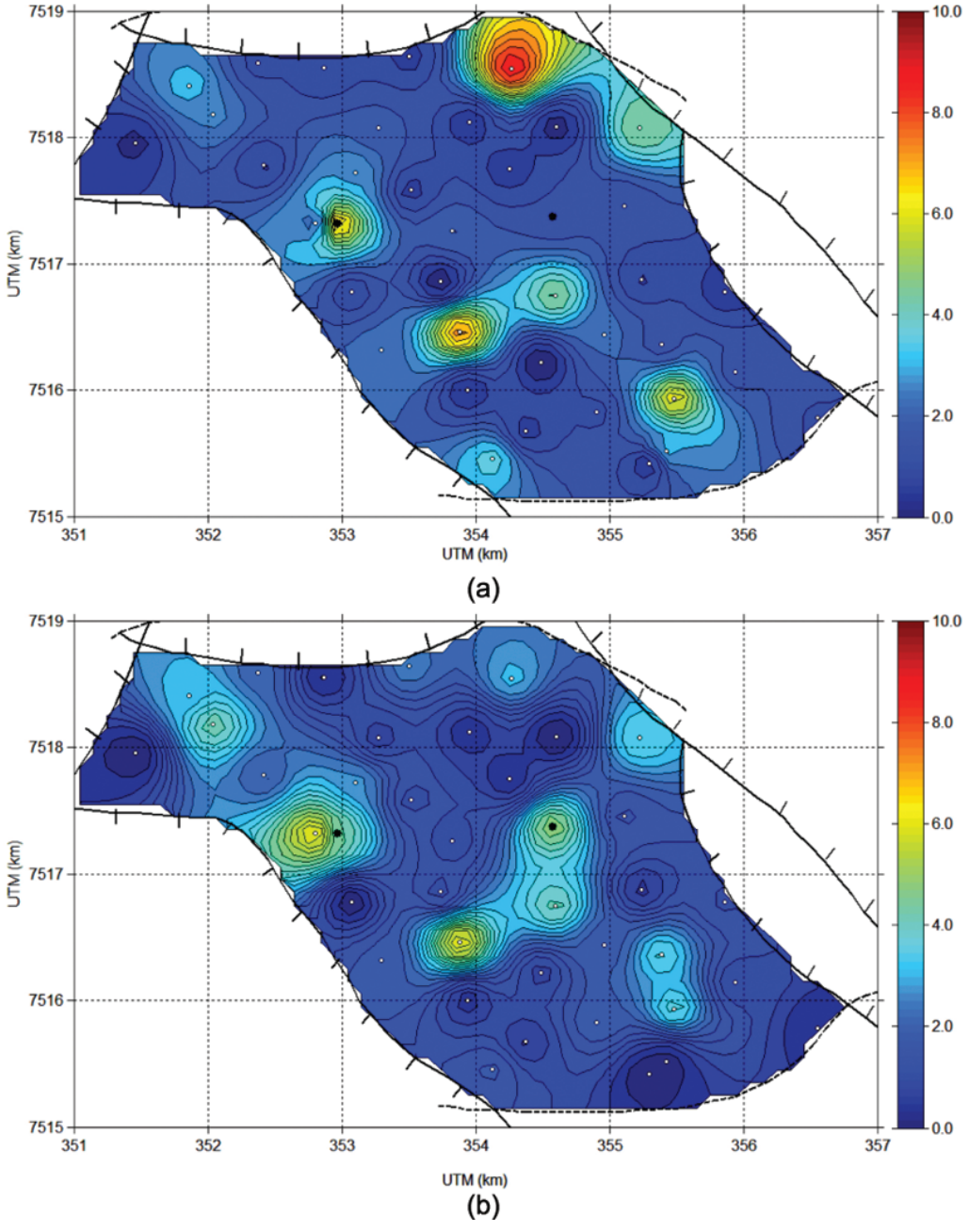

Figura 8 – Absolute relative residuals for EI maps: $\| [\, \mathrm{EI}^{\mathrm{iso}}(\theta) - \mathrm{EI}^{\mathrm{vti}}(\theta) \,]/\mathrm{EI}^{\mathrm{iso}}(\theta) \| \times 100\%$. (a) $\theta = 20°$ and (b) $\theta = 40°$. Filled circles denote reference wells NA 1A and NA 2 (see locations in Figs. 1 and 3). White circles are further wells drilled in the area.

$\mathrm{EI}^{\mathrm{vti}}$ values in three situations: (a) the whole set of control points; (b) the overall EI values estimated in the cell of the grid; and (c) the estimated EI values in the central region of the maps inside a circle with radius of 1.5 km. We note a stable behavior of the statistical measurements in Table 1. Specifically, the small differences in the variance for the generated EI maps reveals a good confidence of the interpolation process of our methodology.

DISCUSSION AND CONCLUSIONS

During the characterization and development of an oil and gas field, the construction of depth maps is the usual procedure for investigating the overall spatial variation of lithotypes physical properties. Interpretation of such depth maps can help identification of layers continuity between wells, with direct impact on the minimization of costs in drilling operations of additional produc-

Table 1 – Statistics for uncertainty analysis of the interpolated EI maps in Figures 5, 6 and 7. Computation of minimum, maximum and mean values for EI (in km/s $\times$ g/cm^3) as well as standard deviation σ and variance σ^2 assumed only: (a) the whole set of control points; (b) the overall points of the grid after interpolation; and (c) the interpolated values in the center of the map inside a circular region with radius of 1.5 km.

	$\theta = 0°$		$\theta = 20°$		$\theta = 40°$	
(a)	EI^{iso}	EI^{vti}	EI^{iso}	EI^{vti}	EI^{iso}	EI^{vti}
EI_{min}	6.98	7.10	6.93	7.12	6.82	7.04
EI_{max}	11.06	10.53	10.53	10.36	11.09	11.44
EI_{mean}	8.65	8.72	8.54	8.53	8.36	8.38
σ	0.93	0.84	0.82	0.79	0.93	0.90
σ^2	0.87	0.71	0.67	0.62	0.86	0.82
(b)	EI^{iso}	EI^{vti}	EI^{iso}	EI^{vti}	EI^{iso}	EI^{vti}
EI_{min}	7.02	7.15	6.96	7.17	6.85	7.08
EI_{max}	11.06	10.52	10.53	10.32	11.08	11.43
EI_{mean}	8.68	8.75	8.57	8.58	8.42	8.44
σ	0.67	0.59	0.60	0.57	0.72	0.70
σ^2	0.45	0.35	0.36	0.33	0.52	0.50
(c)	EI^{iso}	EI^{vti}	EI^{iso}	EI^{vti}	EI^{iso}	EI^{vti}
EI_{min}	7.02	7.21	6.96	7.17	6.85	7.08
EI_{max}	10.83	10.43	10.35	10.32	10.90	11.22
EI_{mean}	8.73	8.74	8.54	8.49	8.21	8.24
σ	0.62	0.52	0.58	0.53	0.68	0.64
σ^2	0.38	0.27	0.34	0.28	0.46	0.41

tion wells. As geophysical measurements at the vicinity of boreholes are a main source of information in the characterization procedures of oil and gas reservoirs, any well-logged or log-derived physical property can serve, in principle, as the inputs in the depth map generation process.

As presented in this paper, the EI concept represents a further petrophysical parameter which can be mapped at selected depths of the reservoir formation under study. The isotropic and anisotropic EI maps generated at 3080 m depth in the Namorado reservoir formation revealed regions of abrupt changes in bulk density and seismic velocities. Specifically, two conclusions can be drawn from inspecting the anisotropic EI maps. The first conclusion is that, as parameters of the anisotropic EI formula, the reference velocities α and β must be selected in order to avoid blurring seismic anisotropy effects. See the interpretation of the $EI^{iso}(0°)$ and $EI^{vti}(0°)$ maps in Figures 5(a) and 5(b), respectively. In order words, it might occur that effects of seismic anisotropy could be attenuated by the choice of non-optimum reference velocities. Though a more detailed study should be taken into account, we consider our choice for α and β as optimum because of the good correlation of the log curves with the geologic column observed in Figure 4. The second conclusion is drawn from inspecting the maps of absolute relative residuals in Figure 8, which shows that fine-layering responds to the very weak VTI anisotropy effects in the Namorado reservoir formation.

Finally, we point out the robustness of the inverse-distance square-weighted interpolator selected in this paper for construction of EI maps. In combination with the search radius scheme, the estimated values of EI remained in between the inputs of the

Namorado well log data set. Analysis of the statistics in Table 1 exhibits variances with low magnitude, confirming the excellent performance of the interpolation scheme. In fact, the investigations in Weber & Englund (1992; 1994) support that inverse-distance interpolators provide results comparable to geostatistical interpolators. Nevertheless, because no account of the spatial correlation distance is taken, inverse-distance interpolators can hardly be considered optimum. This explains our choice for implementing an uncertainty analysis of the EI maps by means of standard statistical measures.

APPENDIX

The first part of this appendix shows the basic relations of the methodology for estimating S-wave velocities proposed in Lee (2006). In the second part, we present the basic steps to obtain Eq. (6) according to the developments in Martins (2006). Further details of both treatments can be found in the listed references.

Shear-wave velocity estimation

In the following, we present the main steps of the methodology proposed by Lee (2006) for estimating S-wave velocity from a P-wave velocity measurement. The methodology starts with the relations for seismic velocities of fluid-saturated porous rocks. For P waves,

$$V_{P,sat}^2 = \frac{\kappa_b + \frac{4}{3}\mu_b}{\rho_b}, \tag{A1}$$

while, for S waves,

$$V_{S,sat}^2 = \frac{\mu_b}{\rho_b}. \tag{A2}$$

The bulk modulus and the shear-wave modulus are represented by κ_b and μ_b, respectively. The bulk density ρ_b is given as

$$\rho_b = (1-\phi)\,\rho_{ma} + \phi\, S_f\, \rho_f, \tag{A3}$$

where ϕ denotes fractional total porosity, while S_f and ρ_f are the fluid saturation and density, respectively. Lee (2006) takes into account the Biot-Gassmann theory (Greenberg & Castagna, 1992) in which the bulk modulus of a fluid-saturated porous rock is related as $\kappa_b \equiv \kappa_{sat}$ as follows

$$\kappa_{sat} = \kappa_d + \frac{[\,1-\kappa_d/\kappa_{ma}\,]^2}{\phi/\kappa_f + (1-\phi)/\kappa_{ma} - \kappa_d/\kappa_{ma}^2}. \tag{A4}$$

In the preceding equation, κ_d, κ_f and κ_{ma} stand for the bulk modulus of the dry rock, the bulk modulus of the fluid and the bulk modulus of the grain minerals in the rock matrix, respectively. For the dry bulk modulus κ_d, Lee (2006) used the definition provided in Pride et al. (2004),

$$\kappa_d = \kappa_{ma}\,\frac{1-\phi}{1+\alpha_c\,\phi}. \tag{A5}$$

As for the shear-wave modulus of the dry rock μ_d, Lee (2006) generalized the definition given in Pride et al. (2004), as follows:

$$\mu_d = \mu_{ma}\,\frac{1-\phi}{1+\gamma_\alpha\,\alpha_c\,\phi}, \tag{A6}$$

where $\gamma_\alpha = (1+2\,\alpha_c)/(1+\alpha_c)$ and μ_{ma} is the shear-wave modulus of the grain minerals in the rock matrix. In Eqs. (A5) and (A6), α_c represents the degree of consolidation between grains.

Using the preceding equations, we can obtain models for P- and S-wave velocities – not shown in Lee (2006). Substituting γ_α into Eq. (A6), the relation for the shear-wave modulus of the dry rock yields

$$\mu_d = \mu_{ma}\,\frac{(1-\phi)\,(1+\alpha_c)}{1+(1+\phi)\,\alpha_c+2\,\phi\,\alpha_c^2}. \tag{A7}$$

In the Biot-Gassmann theory, the porous rock is assumed fully saturated, $S_f = 100\,\%$, yielding $\rho_b \equiv \rho_{sat}$ in Eq. (A3), i.e., $\rho_{sat} = (1-\phi)\,\rho_{ma} + \phi\,\rho_f$. Further, the equivalence $\mu_b \equiv \mu_d \equiv \mu_{sat}$ applies for the shear-wave modulus.

On the other hand, the combination of Eqs. (A4) and (A5) yields a formula for $\kappa_{\rm sat}$. After inserting the resulting formula for $\kappa_{\rm sat}$ and Eq. (A7) into Eq. (A1), it gives the petrophysical model for P-wave velocities in fluid-saturated porous rock,

$$\begin{aligned} \mathrm{V}^2_{\mathrm{P,sat}}(\alpha_{\rm c}) \;\; = \;\; & \frac{1-\phi}{\rho_{\rm sat}} \left[\frac{1}{1+\alpha_{\rm c}\,\phi} \left(1 + \frac{\phi\,(1+\alpha_{\rm c})^2}{(1-\phi)^2\,\alpha_{\rm c} + (1-\phi)\,(1+\alpha_{\rm c}\,\phi)\,\kappa_{\rm ma}/\kappa_{\rm f}} \right) \kappa_{\rm ma} \right. \\ & \left. + \frac{4\,(1+\alpha_{\rm c})}{3\,(1+(1+\phi)\,\alpha_{\rm c} + 2\,\phi\,\alpha_{\rm c}^2)}\,\mu_{\rm ma} \right], \end{aligned} \tag{A8}$$

and also the petrophysical model for S-wave velocities,

$$\mathrm{V}^2_{\mathrm{S,sat}}(\alpha_{\rm c}) = \frac{1-\phi}{\rho_{\rm sat}} \left[\frac{(1+\alpha_{\rm c})}{1+(1+\phi)\,\alpha_{\rm c} + 2\,\phi\,\alpha_{\rm c}^2}\,\mu_{\rm ma} \right]. \tag{A9}$$

The main parameters in Eqs. (A8) and (A9) are defined for clastic sedimentary rocks, in which quartz is the predominant grain mineral. In this way, $\kappa_{\rm ma} = 36$ GPa, $\mu_{\rm ma} = 45$ GPa and $\rho_{\rm ma} = 2.65$ g/cm^3. In this paper, we used P-wave velocity measurements from sonic logs for estimating S-wave velocities. The properties of the saturating fluid correspond to the mud filtrate properties, because the depth of penetration of the sonic logging tool gives slowness measurements within the so-called flushed zone (Dewan, 1983). We then assumed, for the mud filtrate, $\kappa_{\rm f} = 2.65$ GPa and $\rho_{\rm f} = 1.10$ g/cm^3. As for the total porosity, it can be estimated from the available bulk density log.

Inserting the values for $\kappa_{\rm ma}$, $\mu_{\rm ma}$, $\rho_{\rm ma}$, $\kappa_{\rm f}$, $\rho_{\rm f}$ and ϕ into Eqs. (A8) and (A9), we notice the dependence of the petrophysical models for P- and S-wave velocities on the degree of consolidation $\alpha_{\rm c}$. The solution of the equation

$$\mathrm{V}^{\rm mod}_{\rm P}(\alpha_{\rm c}) - \mathrm{V}^{\rm meas}_{\rm P} \approx 0, \tag{A10}$$

where

$$\mathrm{V}^{\rm mod}_{\rm P}(\alpha_{\rm c}) \equiv \sqrt{\mathrm{V}^2_{\mathrm{P,sat}}(\alpha_{\rm c})}$$

and $\mathrm{V}^{\rm meas}_{\rm P}$ stands for measured P-wave velocity converted from the sonic log, yields a value for the degree of consolidation $\alpha_{\rm c}$. The estimation of the S-wave velocity is then obtained by substituting this value for $\alpha_{\rm c}$ into Eq. (A9). As in Lee (2006), we also used the Newton-Raphson method for solving Eq. (A10).

Anisotropic EI equation

The goal of this section is to present the basic relations for evaluating the argument of the correction term in Eq. (5). Following Martins (2006), the weak-contrast approximation for $\mathrm{R_{PP}}$ coefficients in weakly anisotropic media with arbitrary symmetry derived in Vavryčuk & Pšenčík (1998) can be written as

$$\mathrm{R_{PP}}(\varphi,\theta) = \mathrm{R^{iso}_{PP}}(\theta) + \Delta\mathrm{R_{PP}}(\varphi,\theta), \tag{A11}$$

where θ is the angle between the normal to the interface and the phase vector normal to the incident wave front ($\theta = 0^\circ$ for a vertical incidence) and φ is the azimuthal phase angle ($\varphi = 0^\circ$ for direction along x_1 axis). To simplify notation, the subscript PP is used in place of qPqP (i.e., quasi-compressional wave).

In Eq. (A11), $\mathrm{R^{iso}_{PP}}(\theta)$ is the weak-contrast approximation for PP-wave reflection coefficients given in Aki & Richards (1980). The term $\Delta\mathrm{R_{PP}}(\varphi,\theta)$ represents the perturbation to weak anisotropy with arbitrary symmetry, expressed as

$$\Delta\mathrm{R_{PP}}(\varphi,\theta) = \mathrm{A^{ani}}\,\cos^2\theta + \mathrm{B^{ani}}\,\sin^2\theta + \mathrm{C^{ani}}\,\sin^2\theta\,\tan^2\theta. \tag{A12}$$

The terms $\mathrm{A^{ani}}$, $\mathrm{B^{ani}}$ and $\mathrm{C^{ani}}$ contain information on elastic stiffnesses. Only $\mathrm{B^{ani}}$ and $\mathrm{C^{ani}}$ also depend on the azimuthal phase angle φ. It follows that

$$\mathrm{A^{ani}} = \frac{1}{2\bar{\alpha}^2}\,\Delta(\alpha^2\epsilon_z), \tag{A13}$$

$$\mathrm{B^{ani}} = \frac{1}{2\bar{\alpha}^2}\left(\mathrm{B}_1\cos^2\varphi + \mathrm{B}_2\sin^2\varphi + \mathrm{B}_3\sin\varphi\,\cos\varphi\right), \tag{A14}$$

where

$$\mathrm{B}_1 = \Delta(\alpha^2\delta_x) - 8\,\Delta(\beta^2\gamma_x),\ \mathrm{B}_2 = \Delta(\alpha^2\delta_y) - 8\,\Delta(\beta^2\gamma_y)\ \text{ and }\ \mathrm{B}_3 = 2\,[\Delta(\alpha^2\chi_z) - 4\,\Delta(\beta^2\epsilon_{45})].$$

The term $\mathrm{C}^{\mathrm{ani}}$ in Eq. (A12) is related as

$$\mathrm{C}^{\mathrm{ani}} = \frac{1}{2\bar{\alpha}^2}\left(\mathrm{C}_1\cos^4\varphi + \mathrm{C}_2\sin^4\varphi + \mathrm{C}_3\sin^2\varphi\,\cos^2\varphi + \mathrm{C}_4\sin\varphi\,\cos^3\varphi + \mathrm{C}_5\sin^3\varphi\,\cos\varphi\right), \tag{A15}$$

where

$$\mathrm{C}_1 = \Delta(\alpha^2\epsilon_x),\ \mathrm{C}_2 = \Delta(\alpha^2\epsilon_y),\ \mathrm{C}_3 = \Delta(\alpha^2\delta_z),\ \mathrm{C}_4 = 2\,\Delta(\alpha^2\epsilon_{16}),\ \text{ and }\ \mathrm{C}_5 = 2\,\Delta(\alpha^2\epsilon_{26}).$$

In Eqs. (A13)–(A15), the following terminology applies for the relations involving the Δ's:

$$\Delta(\alpha^2\epsilon_z) = \alpha^2_{\mathrm{II}}\,\epsilon_{z,\mathrm{II}} - \alpha^2_{\mathrm{I}}\,\epsilon_{z,\mathrm{I}}\,,\ \Delta(\alpha^2\delta_x) = \alpha^2_{\mathrm{II}}\,\delta_{x,\mathrm{II}} - \alpha^2_{\mathrm{I}}\,\delta_{x,\mathrm{I}},\ \text{etc.}$$

The subscripts I and II denote upper and lower medium, respectively. See below the meaning of parameters ϵ_z, δ_x, etc.

Equations (A13)–(A15) reveal linear dependence of Vavryčuk & Pšenčík (1998) $\mathrm{R_{PP}}$ coefficient approximation on 12 of the whole set of the so-called WA parameters previously defined in Pšenčík & Gajewski (1998) and further in Farra & Pšenčík (2003). Clearly, the $\mathrm{R_{PP}}$ coefficient approximation in Eq. (A11) depends on nine P-wave WA parameters, i.e.,

$$\begin{gathered}
\epsilon_x = \frac{A_{11}-\alpha^2}{2\alpha^2},\quad \epsilon_y = \frac{A_{22}-\alpha^2}{2\alpha^2},\quad \epsilon_z = \frac{A_{33}-\alpha^2}{2\alpha^2},\\[2ex]
\delta_x = \frac{A_{13}+2A_{55}-\alpha^2}{\alpha^2},\quad \delta_y = \frac{A_{23}+2A_{44}-\alpha^2}{\alpha^2},\\[2ex]
\delta_z = \frac{A_{12}+2A_{66}-\alpha^2}{\alpha^2},\quad \chi_z = \frac{A_{36}+2A_{45}}{\alpha^2},\\[2ex]
\epsilon_{16} = \frac{A_{16}}{\alpha^2},\quad \epsilon_{26} = \frac{A_{26}}{\alpha^2},
\end{gathered} \tag{A16}$$

and on three S-wave WA parameters, i.e.,

$$\gamma_x = \frac{A_{55}-\beta^2}{2\beta^2},\quad \gamma_y = \frac{A_{44}-\beta^2}{2\beta^2},\quad \epsilon_{45} = \frac{A_{45}}{\beta^2}. \tag{A17}$$

In the preceding equations, the A_{ij}'s are elements of the density-normalized elastic matrix, while α and β represent P- and S-wave reference isotropic velocities, respectively. Note that the whole set of WA parameters vanishes under assumption of isotropy and if the reference velocities are taken as $\alpha^2 = A_{33}$ and $\beta^2 = A_{44}$.

In this way, the integral in the argument of Eq. (5) can be evaluated by using Eqs. (A13)–(A15), in which, also due to assuming continuous variation of medium properties,

$$\Delta(\alpha^2\epsilon_x)\to d(\alpha^2\epsilon_x),\ \Delta(\alpha^2\delta_x)\to d(\alpha^2\delta_x),\ \Delta(\beta^2\gamma_x)\to d(\beta^2\gamma_x),\ \Delta(\beta^2\epsilon_{45})\to d(\beta^2\epsilon_{45}),\ \text{etc.}$$

Defining $\mathrm{k}_2 = 1/\bar{\alpha}^2$ as a constant quantity, the evaluation of Eq. (5) then yields

$$\begin{aligned}
2\int d\,\mathrm{R_{PP}}(\varphi,\theta) \quad \equiv \quad & \alpha^2\,\mathrm{k}_2\,\{\,\epsilon_z\cos^2\theta + [\,(\delta_x - 8(\beta/\alpha)^2\,\gamma_x)\cos^2\varphi\\
& + (\delta_y - 8(\beta/\alpha)^2\,\gamma_y)\sin^2\varphi + (\chi_z - 4(\beta/\alpha)^2\,\epsilon_{45})\sin 2\varphi\,]\,\sin^2\theta\\
& + [\,\epsilon_x\cos^4\varphi + \epsilon_y\sin^4\varphi + \frac{1}{4}\,\delta_z\,\sin^2 2\varphi\\
& + (\epsilon_{16}\cos^2\varphi + \epsilon_{26}\sin^2\varphi)\sin 2\varphi\,]\,\sin^2\theta\,\tan^2\theta\,\},
\end{aligned} \tag{A18}$$

which is Eq. (6). It holds for weakly anisotropic media of arbitrary symmetry.

ACKNOWLEDGMENTS

This paper presents results of the research project "Caracterização de Anisotropia Sísmica Usando Perfis Geofísicos de Poços de Petróleo e Gás" with financial support from CNPq/Brazil, the Brazilian Agency for the Development of Sci. & Technology (proc. 471647/2006-3). José Oliveira acknowledges the scholarship from CAPES/Brazil, supporting the development of his master dissertation in the Post-graduation Course in Geophysics at Observatório Nacional/Brazil. Comments and suggestions of two anonymous reviewers contributed to improving the final version of this paper.

REFERENCES

ADRIANO LB. 2007. Estimativa de argilosidade e porosidade no reservatório Namorado a partir de perfilagem geofísica de poços. Universidade do Estado do Rio de Janeiro, Faculdade de Geologia, Monografia de Final de Curso, 57 pp. (*In Portuguese*).

AKI K & RICHARDS PG. 1980. Quantitative Seismology – Theory and Methods. W. H. Freeman & Co., Vol. I, Chapter 5, p. 153.

AUGUSTO FOA. 2009. Mapas de amplitude sísmica para incidência normal no reservatório Namorado, bacia de Campos. Post-graduation Course in Geophysics, Observatório Nacional, M.Sc. dissertation, 103 pp. (*In Portuguese*).

AUGUSTO FOA & MARTINS JL. 2008. Relações empíricas não-convencionais para estimativa de perfis sônicos de ondas compressionais. In: Rio Oil & Gas 2008: EXPO and Conference, paper IBP1786_08, CD-ROM. (*In Portuguese*).

AUGUSTO FOA & MARTINS JL. 2009. A well-log regression analysis for P-wave velocity prediction in the Namorado oil field, Campos basin. Brazilian Journal of Geophysics, 27: 595–608.

AUGUSTO FOA, MARTINS JL & SILVA JC. 2007. Compressional-wave velocity variation in the upper Macaé formation: a well-log regression analysis study. In: 10th Intern. Cong. of the Braz. Geophysical Society: Expanded Abstracts, CD-ROM.

BACKUS GE. 1962. Long-wave elastic anisotropy produced by horizontal layering. Journal of Geophysical Research, 67: 4427–4440.

BAYUK IO, AMMERMAN M & CHESNOKOV EM. 2008. Upscaling of elastic properties of anisotropic sedimentary rocks. Geophysical Journal International, 172: 842–860.

CASTAGNA JP, BATZLE ML & KAN TK. 1993. Rock physics: The link between rock properties and AVO response. In: CASTAGNA JP & BACKUS MM (Eds.). Offset-dependent reflectivity – Theory and practice of AVO analysis. Investigations in Geophysics no. 8, Society of Exploration Geophysicists, 135–171.

CASTAGNA JP, SWAN HW & FOSTER DJ. 1998. Framework for AVO gradient and intercept interpretation. Geophysics, 63: 948–956.

CONNOLLY P. 1998. Calibration and inversion of non-zero offset seismic. In: 68th Ann. Internat. Mtg. SEG: Expanded Abstracts, 182–184.

CONNOLLY P. 1999. Elastic Impedance. The Leading Edge, 18: 438–452.

DEWAN JT. 1983. Essentials of modern open-hole log interpretation. PennWell Books, 361 pp.

ELLIS DV & SINGER JM. 2007. Well logging for Earth scientists. 2nd edition. Springer, 692 pp.

FARRA V & PŠENČÍK I. 2003. Properties of the zeroth-, first-, and higher-order approximations of attributes of elastic waves in weakly anisotropic media. Journal of Acoustical Society of America, 114: 1366–1378.

GREENBERG ML & CASTAGNA JP. 1992. Shear-wave velocity estimation in porous rock: Theoretical formulation, preliminary verification and applications. Geophysical Prospecting, 40: 195–209.

HELBIG K. 1994. Foundations of Anisotropy for Exploration Seismics. Pergamon Press, 483 pp.

LARIONOV WW. 1969. Borehole Radiometry. Nedra, 127 pp. (*In Russian*).

LEE MW. 2006. A simple method of predicting S-wave velocity. Geophysics, 71: F161–F164.

LINER CL & FEI TW. 2006. Layer-induced seismic anisotropy from full-wave sonic logs: theory, application and validation. Geophysics, 71: D183–D190.

MARTINS JL. 2003. A second-order approach for P-wave elastic impedance technology. Stud. Geophys. Geod., 47: 545–564.

MARTINS JL. 2006. Elastic impedance in weakly anisotropy media. Geophysics, 71: D73–D83.

MARTINS JL. 2008. Compressional-wave elastic impedance in TI media. In: Proceedings of the 13th Intern. Workshop on Seismic Anisotropy, August 10-15, Winter Park, CO, 89–90.

MENSCH T & RASOLOFOSAON P. 1997. Elastic wave velocities in anisotropic media of arbitrary symmetry – Generalization of Thomsen's parameters ϵ, δ, and γ. Geophysical Journal International, 128: 43–64.

MITCHUM RM, VAIL PR & THOMPSON S. 1977. Seismic stratigraphy and global changes of sea level, part 2: the depositional sequence as a basic unit for stratigraphic analysis. In: PAYTON CE (Ed.). Seismic stratigraphy: applications to hydrocarbon exploration, Memoir 26, American Association of Petroleum Geologists, 53–62.

POSTMA GW. 1955. Wave propagation in a stratified medium. Geophysics, 20: 780–806.

PRIDE SR, BERRYMAN JG & HARRIS JM. 2004. Seismic attenuation due to wave-induced flow. Journal of Geophysical Research, 109: B01201.

PŠENČÍK I & GAJEWSKI D. 1998. Polarization, phase velocity and NMO velocity of qP waves in arbitrary weakly anisotropic media. Geophysics, 63: 1754–1766.

RUTHERFORD SR & WILLIAMS RH. 1989. Amplitude-*versus*-offset variations in gas sands. Geophysics, 54: 680–688.

STOVAS A, LANDRØ M & AVSETH P. 2006. AVO attribute inversion for finely layered reservoirs. Geophysics, 71: C25–C36.

TIGRE CA & LUCCHESI CF. 1986. Estado atual do desenvolvimento da Bacia de Campos e perspectivas. In: Seminário de Geologia de Desenvolvimento e Reservatório, DEPEX-PETROBRAS, Rio de Janeiro, 1–12. (*In Portuguese*).

TIWARY DK, BAYUK IO, VIKHOREV AA & CHESNOKOV EM. 2009. Comparison of seismic upscaling methods: from sonic to seismic. Geophysics, 74: WA3–WA14.

VAVRYČUK V & PŠENČÍK I. 1998. PP-wave reflection coefficients in weakly anisotropic media. Geophysics, 63: 2129–2141.

VERWEST B. 2004. Elastic impedance revisited. In: Proceedings of the 66th EAGE Conference & Exhibition: Expanded Abstracts, Paper P342. CD-ROM.

VERWEST B, MASTERS R & SENA A. 2000. Elastic impedance inversion. In: Proceedings of the 70th Intern. SEG Meeting: Expanded Abstracts, 1580–1582.

WEBER DD & ENGLUND EJ. 1992. Evaluation and comparison of spatial interpolators. Mathematical Geology, 24: 381–391.

WEBER DD & ENGLUND EJ. 1994. Evaluation and comparison of spatial interpolators II. Mathematical Geology, 26: 589–603.

WHITCOMBE DN. 2002. Elastic impedance normalization. Geophysics, 67: 60–62.

WORTHINGTON PF. 1985. The evolution of shaly-sand concepts in reservoir evaluation. The Log Analyst, 26: 23–40.

YILMAZ O. 2001. Seismic data analysis: processing, inversion, and interpretation of seismic data. 2nd edition. In: DOHERTY SM (Ed.). Soc. Expl. Geophysicists, Volumes I–II, 2027 pp.

NOTES ABOUT THE AUTHORS

José Sampaio de Oliveira holds a B.S. degree (2007) in Physics from Universidade Federal Fluminense, Brazil. He earned his master dissertation (May 17th, 2010) in the Post-graduation Course in Geophysics at Observatório Nacional, Ministry of Science and Technology, Brazil. He is a member of SBGf.

Jorge Leonardo Martins holds a B.S. degree (1986) in Civil Engineering from Universidade Veiga de Almeida and a Ph.D. (1992) in Applied Geophysics from Universidade Federal da Bahia, Brazil. He was an associate researcher at Universidade Estadual do Norte Fluminense (1993-1998), visiting researcher at the Geophysical Institute of the Czech Acad. of Sci. (April-June/1998), post-doctoral fellow at the SW3D Consortium Project (August/1998-January/2000), visiting researcher at Universidade Estadual de Campinas (2000), associate researcher at the Pontifícia Universidade Católica do Rio de Janeiro (2001), and visiting professor at Universidade do Estado do Rio de Janeiro (2002). Currently, he holds an associate researcher position at Observatório Nacional, Ministry of Science and Technology, Brazil. His professional interests include theory and practice of seismic anisotropy, azimuthal AVO analysis, integration of seismics with well log petrophysics, multicomponent seismics, and seismic data processing. He is a member of SEG and SBGf.